Contrast-detail analysis of three flat panel detectors for digital radiography

Giovanni Borasi[a)]
Servizio di Fisica Sanitaria, Azienda Ospedaliera Santa Maria Nuova, V.le Risorgimento 80, 42100 Reggio Emilia (RE), Italy

Ehsan Samei
Duke Advanced Imaging Laboratories, Departments of Radiology, Physics, and Biomedical Engineering, and Medical Physics Graduate Program, Duke University, DUMC 3302, Durham, North Carolina 27710

Marco Bertolini
Servizio di Fisica Sanitaria, Azienda Ospedaliera Santa Maria Nuova, V.le Risorgimento 80, 42100 Reggio Emilia (RE), Italy

Andrea Nitrosi
Servizio di Fisica Sanitaria, Azienda Ospedaliera Santa Maria Nuova, V.le Risorgimento 80, 42100 Reggio Emilia (RE), Italy

Davide Tassoni
Servizio di Fisica Sanitaria, Azienda Ospedaliera Santa Maria Nuova, V.le Risorgimento 80, 42100 Reggio Emilia (RE), Italy

(Received 26 September 2005; revised 6 March 2006; accepted for publication 7 March 2006; published 17 May 2006)

In this paper we performed a contrast detail analysis of three commercially available flat panel detectors, two based on the indirect detection mechanism (GE Revolution XQ/i, system A, and Trixell/Philips Pixium 4600, system B) and one based on the direct detection mechanism (Hologic DirectRay DR 1000, system C). The experiment was conducted using standard x-ray radiation quality and a widely used contrast-detail phantom. Images were evaluated using a four alternative forced choice paradigm on a diagnostic-quality softcopy monitor. At the low and intermediate exposures, systems A and B gave equivalent performances. At the high dose levels, system A performed better than system B in the entire range of target sizes, even though the pixel size of system A was about 40% larger than that of system B. At all the dose levels, the performances of the system C (direct system) were lower than those of system A and B (indirect systems). Theoretical analyses based on the Perception Statistical Model gave similar predicted SNR_T values corresponding to an observer efficiency of about 0.08 for systems A and B and 0.05 for system C. © *2006 American Association of Physicists in Medicine*. [DOI: 10.1118/1.2191014]

Key words: diagnostic radiology, digital imaging, image quality, flat panel detectors, contrast detail, observer performance

I. INTRODUCTION

For well over a decade, detectors based on photostimulated luminescence (computed radiography—CR),[1,2] charge coupled devices (CCD),[3,4] and photoconduction (Thoravision)[5,6] have been used to acquire x-ray radiography digital images. In the last few years, significant scientific and technological efforts have been devoted to the development of flat panel detectors (FPD).[7] FPD systems consist of a detection layer deposited over an active matrix array (AMA) of thin film transistors (TFT). They are classified as either direct[8,9] or indirect[10,11] types depending on the characteristics of the detection layer.

In the direct conversion detector, radiation quanta are absorbed into a photoconductor layer, most commonly amorphous Selenium, producing electron-hole pairs. Under the influence of a strong electric field created between the external surfaces, the charges are separated, drifted toward the collecting electrodes of the TFT, and then locally stored. After the exposure, a read-out circuit selectively discharges each single TFT to form a single corresponding image element (i.e., pixel). In the indirect conversion, a layer of scintillation material (e.g., CsI:Tl) absorbs the impinging x-ray photons. The light produced is channeled to a photodiode array where it is converted into an electric charge. The following steps of the process are similar to the direct conversion systems.

Compared to conventional screen-film (SF) and CR systems, either type of FPD system offers a potentially higher quantum conversion efficiency. FPD technology enables the acquisition of images with higher quality without increasing patient dose, or alternatively, the acquisition of images with equivalent quality at reduced patient dose. These systems further simplify the radiological workflow, and enable new applications such as flat-panel fluoroscopy,[9] double energy,[12] and three-dimensional imaging procedures.[13]

The performance of some direct and indirect FPD systems for general radiography has been previously studied, focusing mostly on the comparison of a single FPD with more

TABLE I. The imaging systems and their characteristics.

System	Equipment	FPD	Detector material	Nominal thickness (mm)	Pixel pitch (size) (m)	Array size	Imaging area (m^2)
A	General Electric Medical Systems (GE), Revolution XQ/I	GE Revolution	CsI (Tl)	0.500	0.200	2048×2048 single panel	41×41
B	Philips Medical Systems (Ph), Digital Diagnost	Trixell Pixium 4600	CsI (Tl)	0.500	0.143	3001×3001 4 sub-panels	43×43
C	Hologic DirectRay, DR 1000	Direct View DR 1000	a:Se	0.500	0.139	2560×3072 90° tilt table	35×43

traditional detectors (SF or CR). Prior studies were based on physical image quality parameters—(MTF), (NPS), and (DQE),[14,15] psychophysical tests like contrast detail (CD) analysis,[16–18] or both in the context of an observer perception model.[19,20] In recent years, the two groups of research presenting this paper were involved in the evaluation of three commercially available FPD systems. One group based their evaluation on the physical image quality parameters (MTF, NPS, and DQE),[21,22] while the other measured the physical and psychophysical (CD analysis) image quality parameters.[23] In spite of a general qualitative agreement between the results of the evaluations, the difference in experimental conditions and evaluation methodologies made it difficult to quantitatively compare the reported results. Ideally, a complete performance evaluation of the systems should include both physical and psychophysical evaluations in the same standard conditions.

This paper reports on a new cooperative CD experiment of the three FPD systems. The new investigation was made using a commonly utilized phantom and standard exposure conditions.[22] CD curves of the systems were obtained using a (4AFC) methodology, and the experimental CD curves of the systems were compared with theoretical predictions of a perception statistical decision theory observer model based on physical parameters,[24,25] extended to softcopy image evaluations.[26]

II. MATERIALS AND METHODS

A. Imaging systems and x-ray techniques

The main characteristics of the FPD systems are summarized in Table I. System A was installed in the Radiology Department at the Umberto I Hospital (Ancona, Italy), system B at Santa Maria Nuova Hospital (Reggio Emilia, Italy), and system C at Quirinale Clinic in Rome (Rome, Italy). These systems were used to acquire images of a commercially available contrast-detail phantom (CDRAD, Nuclear Associates).[27] This phantom (Fig. 1) is made of an acrylic (Perspex-Polymethyl Methacrylate) support (8 mm thick) in which circular flat-topped holes (discs-targets) are drilled in a square region of about 15×15 mm^2 ("insert"). The size and depth of the holes vary logarithmically within 0.32 to 8.00 mm (±0.02 mm) range along the phantom's structured rows and columns. Starting from the fourth row (target diameters equal or less than 4 mm), each insert contains an additional target positioned randomly in one of the four corners, allowing one to perform a four-alternative forced choice (4-AFC) detectability experiment. In this phantom, the contrast varies very slowly between adjacent details of the same size. The ratio between a target depth and its adjacent target (at lower depth) is $2^{-1/3}$. The small attenuation produced by the targets implies a linear relationship between the targets' depth and contrasts (as discussed below) so that both the depth and the contrast are reduced to half of their initial values every three target steps.

B. Image acquisition

In order to compare physical (MTF, NPS, DQE) and psychophysical (contrast-detail curves) image quality param-

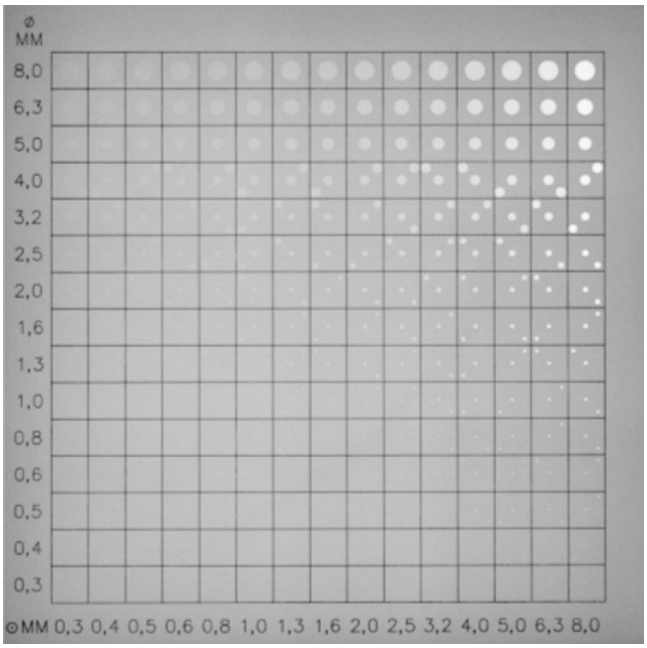

FIG. 1. The CDRAD phantom used for the comparison of the systems.

eters, we adopted a geometrical configuration as similar as possible to that used for physical parameter evaluation. Exposures were made using (IEC RQA5)[28] standard x-ray beam quality at 74 kV, 21 mm Al additional filtration, 7.1 mm Al half value layer (HVL), and, 30 174 $mm^{-2}\,mGy^{-1}$ ideal squared signal-to-noise ratio (SNR_{in}^2) per air kerma. The aluminium absorber was positioned near the tube exit window and maximum allowed source-to-image distance (SID) was selected (183 cm for system A and C and 175 cm for system B). The air kerma values were measured at mid SID and then referred to the detector surface using the inverse square law ("air reference exposure"). Exposure values were measured employing a calibrated dosimeter (PMX III™, RTI, Göteborg, Sweden).

All the systems were calibrated without grid. The phantom was positioned directly over the FPD without any grid interposed. This condition was preferred since the focus of the study was the difference in the basic performance of the detectors as represented by their basic inherent quality metrics (i.e., MTF, NPS, and DQE); grids used by the competing radiological systems had different physical characteristics, introducing additional differences between the systems. Furthermore, the scattered radiation produced by the phantom could be assumed to be reasonably low and similar for the three systems.

The "post phantom" radiation dose impinging on the FPD detector was evaluated from the air reference exposure, by applying a correction factor taking into account the attenuation produced by a 8 mm Perspex layer (equivalent to the CDRAD phantom but without holes) and using the same "broad beam" geometry (35×35 cm^2 field) used for the image acquisition. The transmission factor (T) measured with the PMX III™ radiation detector positioned between the Perspex layer and the FPD was found to be 0.915 ± 0.002 (standard error). This transmission factor refers essentially to the forward directed radiation. In fact, the posterior wall of the PMX III™ included different metallic layers that make the device nearly insensitive to the backscattered radiation ($<2\%$ at this energy).

Comparing "broad" and "narrow" beam attenuation factors for the same Perspex layer, we further evaluated the contribution of scattered radiation in terms of the primary transmission factor Tp, measured to be 0.822 ± 0.002, and the scatter-to-primary ratio (SPR), measured to be 0.097 ± 0.002. The estimated value for the SPR was reasonably close to that reported in the literature.[18,19] From these data, the maximum contrast in CDRAD phantom images (where the layer is drilled from one side to the other) was estimated to be 0.197 ± 0.002, which was in reasonable agreement with the value actually found in the images (0.18–0.19).

For each system, three post-phantom exposure levels ("air kerma") were used: low (about 1 μGy), intermediate (about 2.5 μGy), and high (about 10 μGy), acquiring five images at each exposure level. After each exposure, the phantom was repositioned centrally with respect to the x-ray beam and roughly with respect to the four corners of a 3 mm side square, centered on the beam axis. This repositioning technique was used to avoid having a small detail always imaged at the same location in the detector area. The range of exposure values in the study was chosen based on a prior examination of exposures in clinical radiographic examinations with (DR) systems showing detector air kerma values corresponding to anatomic structures within a 0.5–6 μGy range.

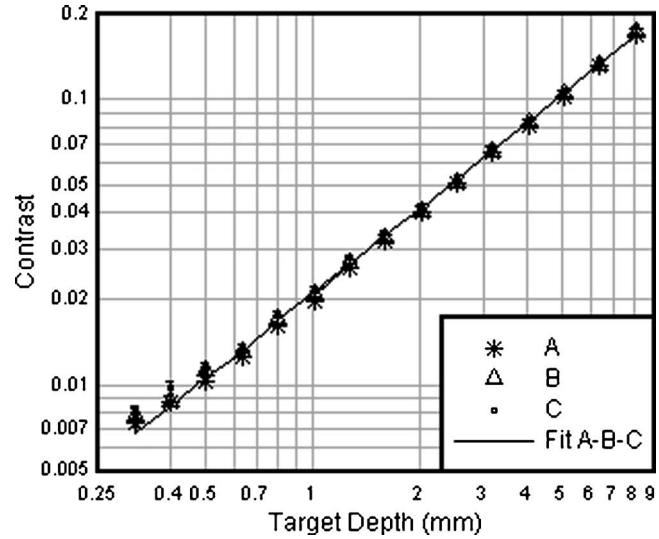

FIG. 2. Image contrasts of the phantom's deepest hole as a function of the hole depth for the three systems. The continuous curve refers to the fitting of the pooled data. The target contrasts are the physical contrasts (formula 3 in the Appendix) directly obtained, without any correction, from the image pixel values.

For all the systems, the gain, offset, and preprocessing settings, including homogeneity and bad pixel corrections, were identical to those used in the clinical operation. An operating mode with no postprocessing and a linear pixel value-exposure response was used for all data acquisitions. For each system, the system response was evaluated within a large exposure range (about 0–60 μGy). Pixel values were determined as an average over a 11.22 mm^2 square area in the middle of the largest and deepest phantom hole/object (diameter=8 mm, depth=8 mm). The response curves relating air kerma and pixel value exhibited a linear behavior with a very high correlation coefficient at each beam quality (i.e., $r_A^2=0.9997$, $r_B^2=0.9999$, $r_C^2=0.9983$).

The contrasts of the largest details of the CDRAD phantom obtained with the three systems and directly evaluated from image digital data, correlated closely with the hole depth, as shown in Fig. 2. In this figure, obtained at 20 μGy, the experimental points refer to the large area target contrasts, defined as $C=\Delta I/I_o$, where ΔI is the variation of the mean signal between every target of the first row (diameter =8 mm) and the surrounding background, and I_o is the mean of the surrounding background signal. The target signal was obtained as the average over a 11.22 mm^2 square (ROI) in the middle of the circular region, while the mean surrounding background signal was estimated by averaging four regions of the same size, located near the corners of the corresponding target square. The data reported in Fig. 2 are the average over five images. Any mention to the target contrast

in the following refers to the contrast evaluated with the linear fit to the data shown in Fig. 2, averaged across systems ($C=\mu\cdot x$, $r=0.997$, $\mu=2.198\cdot 10^{-2}\pm 2.330\cdot 10^{-4}$ mm^{-1}).

C. Observer performance experiment

The images were presented on a five mega pixel (2048 $\times$2560), 540 mm diagonal, diagnostic quality monochrome liquid crystal display (LCD) monitor for softcopy reading (EIZO RadiForce G51-BLS, 165 μm pixel size, 600:1 luminance ratio, 450 cd/m^2 maximum luminance). The system was calibrated according to the (IEC) protocol.[29] The operating conditions, including the phantom background level s and the display contrast enhancement factor γ [see Eq. (A12)], were chosen to achieve the best possible observer performance. The background level ($s=50$ on the 0–255 digital scale) corresponded to a luminance of about 80 cd/m^2. The image contrast γ was set equal to 30. With these settings, the top of the largest and the deepest target resulted in a digital value of about 200, corresponding to a luminance of about 320 cd/m^2. In these conditions, the influence of the eye's internal noise was expected to be negligible, as discussed below. All images were presented on the monitor with the room light off using a 1.5 zoom factor. With this zoom factor, the diameter of the phantom's smallest detail (0.32 mm) corresponds to about three display pixels.

To help the observer in (CD) image evaluation, we developed a new graphical user interface (GUI) using (IDL) (RSI, Pearl East Circle Boulder, CO). The GUI (Fig. 3), which includes a mathematical description of the CDRAD phantom, allows (a) reading and registering of the image files, (b) selecting the insert to be visualized, and (c) choosing the vertex where the additional target is expected to be present. To evaluate the different noise pattern and to reduce the observer's memory effect, after each scoring, the next target is randomly sampled from the (five) repeated images at the same exposure as well as randomly rotated by an angle of 90, 180, or 270 deg. The GUI interface includes push buttons pointing to the four corners and an extra button assigning a 25% probability to each corner during repetitions. Different from other visualization programs proposed in literature[30] for CD analysis with the 4-AFC method, in our case, every phantom detail is presented automatically with little manual adjustment.

Six experienced observers evaluated the image set representing three systems and three dose levels. Before each session, the observer practiced for about 10 min on a simulated image in the same conditions as the real experiment. There was no restriction on viewing time for each decision trial, and observers were given no feedback about whether their decisions were correct after they had been made. All targets were viewed in an order of decreasing contrast. In the perceptibility "transition region," each target evaluation was repeated a fixed number of times ($R=20$) by each observer.

The "transition region" was defined as the region within which the statistical nature of perceptibility is apparent. This region was operatively defined in the following way. For each size, the phantom targets were viewed in a decreasing contrast order and when the observer was absolutely sure that the target was present, the adjacent detail at lower contrast was then considered. This procedure was repeated until the target perceptibility started to decline. At this point, the observer began to "play," trying to find the correct corner where the target might be present. If in R consecutive trials (with the target sampled and rotated at random each time) the correct answer was rendered, the adjacent target at lower contrast was considered. Furthermore, if one or more targets were missed at any of the steps, the observer was directed to go back to the second highest detail to assure a 100% score in two adjacent details immediately before the target level at which the misses occurred. Using this procedure, the perceptibility "transition region" can be defined as a region in which contrasts of the targets fall between total miss and 100% hits.

Each observer scored every detail repeatedly progressively toward the lower contrasts. To help him in the low contrast region (and accelerating the statistical convergence), the GUI included a selectable feature assigning a 25% probability to target presence at each corner during the repetitions. Decreasing the target contrast, most observers made an increased use of this feature. When the observer repeated this choice R times on two adjacent details, the scoring of that detail row was considered completed. Using this protocol, the detection threshold was defined as the lowest contrast of the perceptibility "transition region" of two adjacent targets for which the observer was uncertain about the target location. The (normalized) scores obtained for details in this contrast interval were used to define the (psychometric) detection curve.

Considering 6 observers, 3 systems, 3 dose levels, and 12 target sizes per image, the whole work involved the elaboration of 648 detection (psychophysical) curves and 54 CD curves. The visualization time required to form a single CD curve was about half an hour.

D. Contrast detail data analysis

The detection or psychometric function is a typical example of an observer response: defined as the frequency of the correct response (f_k) versus the disk contrast (C_k), reported in Fig. 4, using a Weibull function,[31] the experimental data were fitted to determine the contrast threshold corresponding to a perception probability of $p_0=0.75$ for each target diameter d. The resulting CD curves of the systems were compared at three standard exposure levels of 1, 2.5, and 10 μGy. To take the exposure variability out of consideration, we applied a correction factor equal to the square root of the ratio between the reference exposure and the measured one.[32]

To verify the statistical significance of the differences between contrast detail curves of the three systems, we first tested, for each target size, the distribution characteristics of the (75%) contrast thresholds using the Kolmogorov-Smirnov one-sample test for normality.[33] In agreement with an earlier work,[34] we verified that the data transformation with natural logarithms conformed to the two conditions of

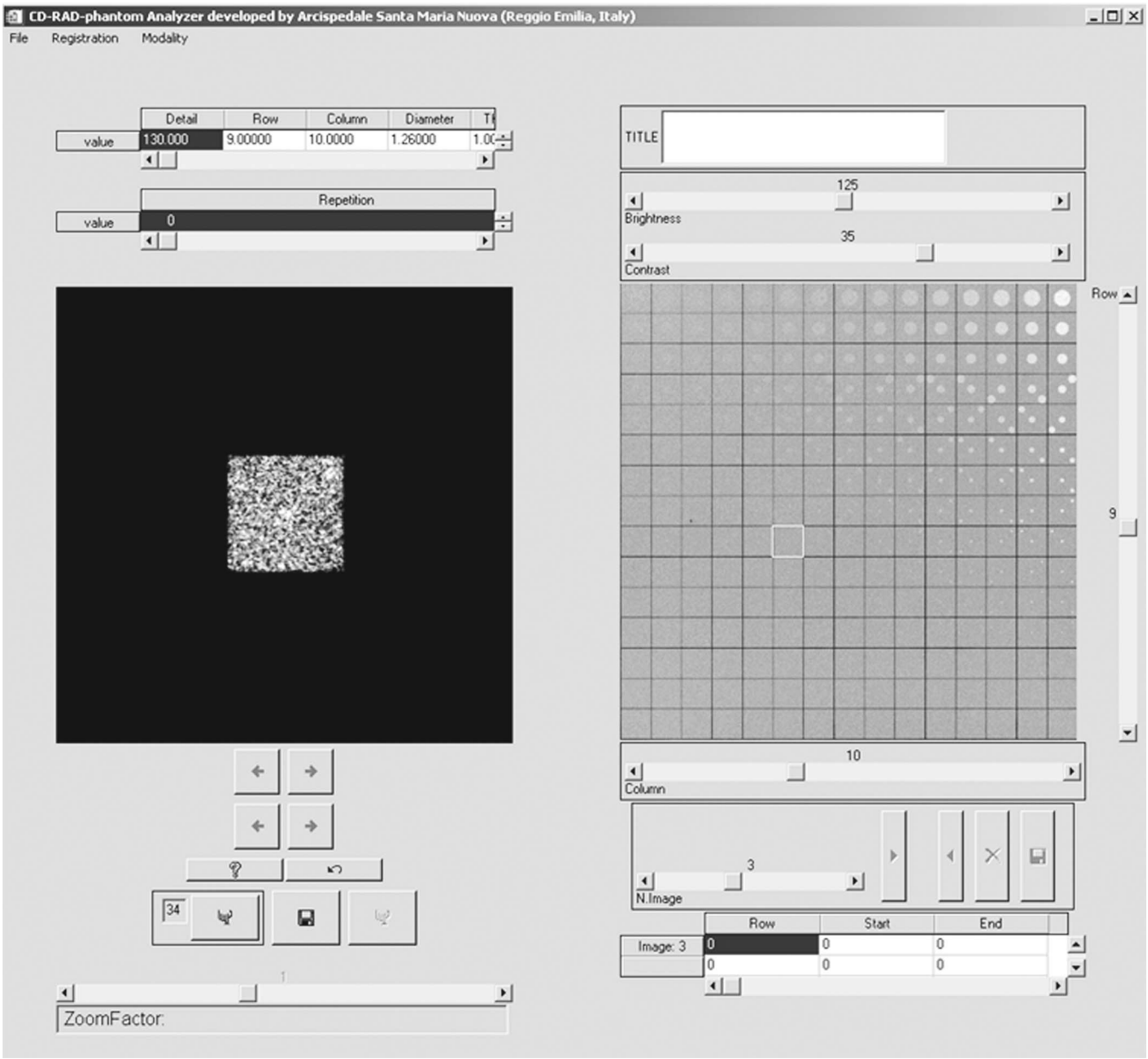

FIG. 3. The main panel of the evaluation program. On the right, from the top: sliding cursors for window contrast and level setting, the reference phantom image, a sliding cursor for image selection, and two sliding cursors for detail selection. The selected detail is visualized on the left side in the middle of a dark area. Under it, four push buttons allow the corner selection. Observer choices are stored and transferred to an EXCEL file for subsequent evaluation.

normality and homogeneity of variance (homoscedasticity). Statistical significance of differences between the three digital systems was assessed with the two-factor analysis of variance (ANOVA)[35] using the logarithmically transformed 75% contrast thresholds as a dependent variable. The main effects considered were detector type and disk size. A p value of less than 0.05 was considered to show a statistically significant difference. The statistical tests were performed with a statistical application package (SPSS version 12.0, SPSS Inc., Chicago, IL).

The analysis was initially performed considering all the phantom targets together. To have a better insight on the effect of the detail size on the detection performance, we further considered the smallest targets (size 0.4–0.32 mm) alone.

E. Theoretical model

A theoretical analysis was performed to determine the expected performance of the three systems. The main aspects of the theoretical model are presented in the Appendix. As discussed there, comparing theoretical and experimental CD curves would require the knowledge of several physical and psychophysical quantities (resolution, noise, and response

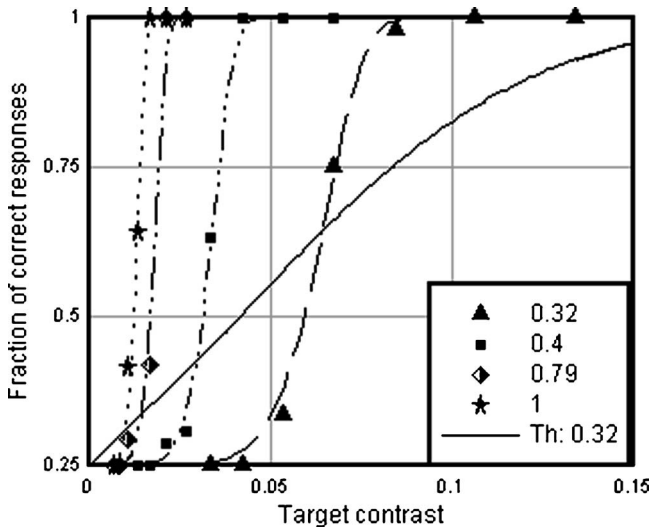

FIG. 4. An example of observer performance (detection or psychometric functions) versus disk contrast in a 4AFC experiment (system B, lowest dose, operator number five). Different curves correspond to different target sizes. The symbols correspond to the experimental data. The dotted and dashed curves between points are obtained by fitting data with the Weibull function described in the text. The continuous curve with a lower slope is obtained by fitting 0.32 mm disk data with the theoretical function for the 4AFC experiment.

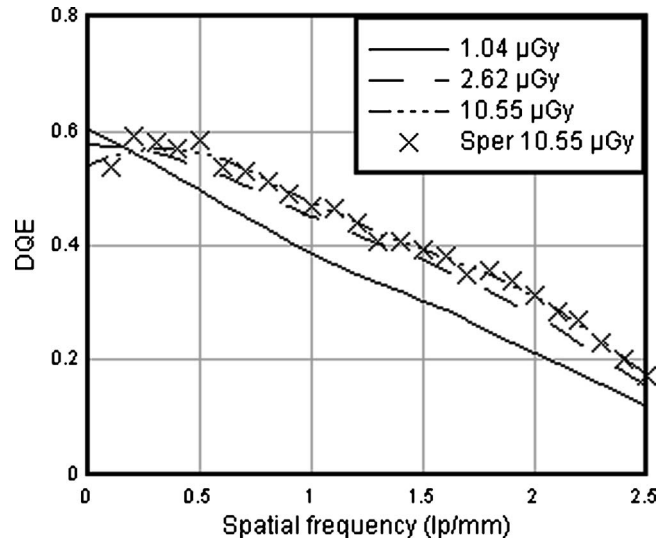

FIG. 6. DQE values (average of the two orthogonal evaluations) of system A (GE) at three different doses. Crosses represent experimental data.

function of the imaging display, and human visual systems). Following Eq. (A5) of the Appendix, theoretical CD curves were fitted to experimental data using a nonlinear least-squares method (Marquardt algorithm).[36]

Required for the theoretical analysis, for all the systems, MTF, NPS, and DQE data were obtained according to the IEC protocol 62220-1.[29] Considering the radial symmetry of these quantities, the curves obtained along the two orthogonal directions were averaged. Figure 5 shows the presampled MTFs of the systems: system B and C curves show an evident "low frequency drop" (LFD).[37] The DQEs of the three systems are reported in Figs. 6–8. The reported data were obtained by smoothing the original samples using the "loess" function included in the Mathcad™ mathematical package. The smoothing parameter (span) was 0.6. In each figure, a sample of the unprocessed data is reported to give an idea of the smoothing effect.

The measured MTF and DQE the systems were in a reasonable agreement with previously published data.[14,22,23,38,39] The monitor effect was accounted for including in the SNR calculation [Eq. (A8) of the Appendix] an estimation of the monitor MTF. Blume *et al.* work[40] reports that LCD monitors exhibit a nearly ideal MTF up to the Nyquist frequency. So we assumed that our monitor's presampled MTF would be reasonably close to a sinc function, corresponding to an ideal square (0.165×0.165 mm^2) aperture.

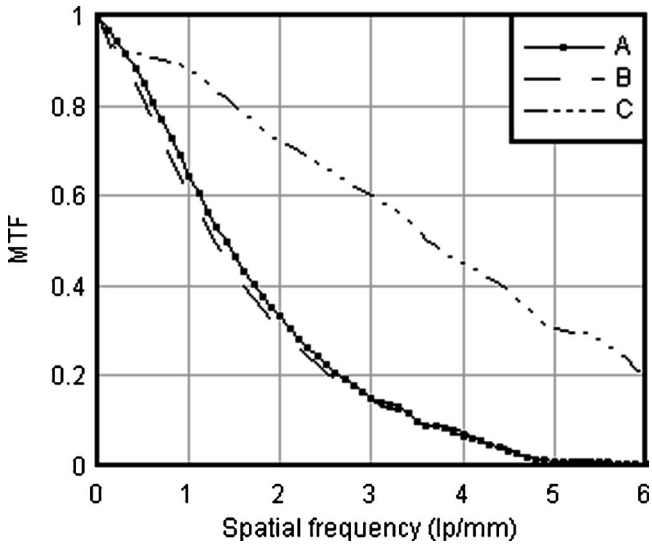

FIG. 5. Presampled MTFs (average of the two orthogonal evaluations) of the three systems (A:GE, B: Philips and C: Hologic).

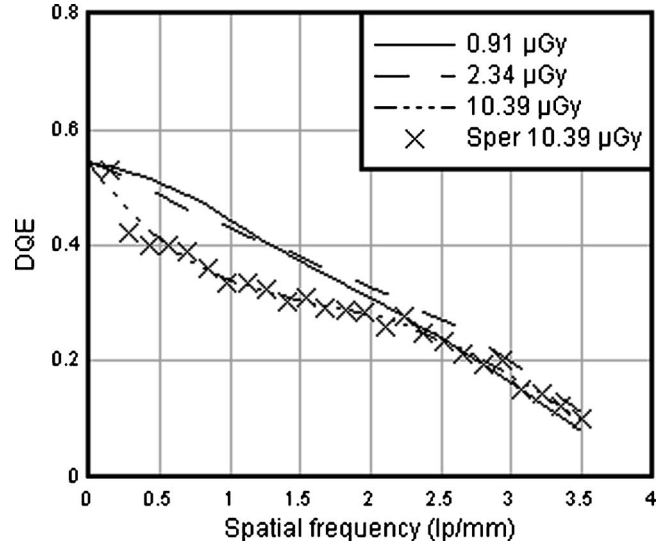

FIG. 7. DQE values (average of the two orthogonal evaluations) of system B (Philips) at three different doses. Crosses represent experimental data.

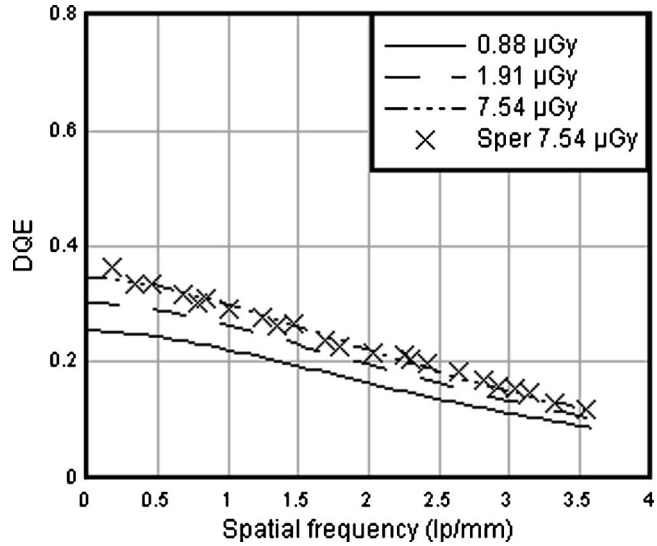

FIG. 8. DQE values (average of the two orthogonal evaluations) of system C (Hologic) at three different doses. Crosses represent experimental data.

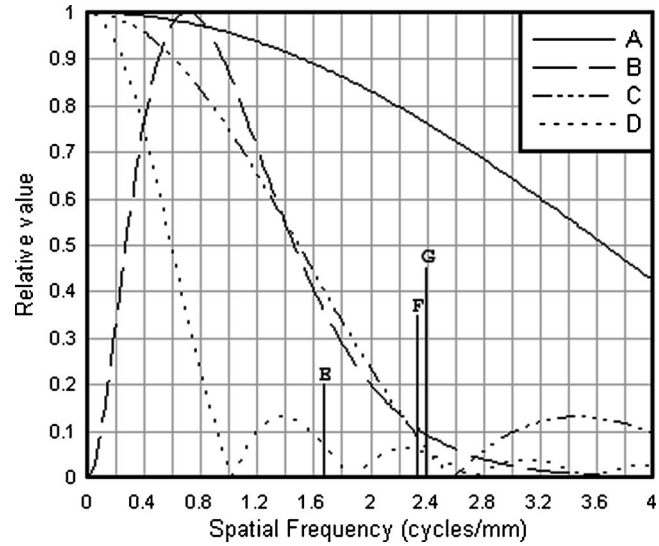

FIG. 9. Blurring effect of different components of the detection chain at the monitor surface (zooming effect included). (a) and (b) represent the monitor and HVS MTFs; (c) and (d) the absolute value of the Fourier transform of the image signal for 0.32 and 0.8 mm size phantom disks (actually 0.48 and 1.2 mm size on the monitor plane). The vertical lines (e), (f), and (g) represent the Nyquist frequency limit respectively for detector A (GE), B (Philips), and C (Hologic).

The theoretical analysis also required a model for the MTF of the human visual system (HVS). Among the models considered (Van Nes and Bouman,[41] Kelly,[42] and Barten[43]), we adopted one proposed by Kelly as it was found to give the best overall correspondence in the shape of the CD curves between theory and experiment. Kelly represents the eye contrast sensitivity with a functional form of $k_1 u^2 \exp \times(-u/k_2)$, where u is the spatial frequency in cycles/degree (Fig. 12 in the Ref. [42]), for an image of 8° and an eye luminance of 1300 trolands (td) (corresponding to 184 cd/m^2 of display luminance and a pupil diameter of 3 mm). A good fit of the solid curve in the above-mentioned figure is obtained with $k_1=0.605$ and $k_2=1.748$. The same function was also adopted by Aufrichtig[19] and Aufrichtig and Xue.[20] The reference curve, expressed in the original paper in terms of cycles/degree, was converted to cycles/mm taking into account the mean visualization distance of 427.5 mm and a zooming factor of 1.5.

The blurring effect of the different components of the detection chain (detector, HVS, monitor) is compared in Fig. 8 with the (normalized) Fourier transform of contrast profile of two targets (0.32 and 0.8 mm in diameter). This comparison takes into account the adopted 1.5 zooming factor (0.48 and 1.2 mm magnified diameter). The MTFs of the detector and the HVS are the most important factors limiting the targets frequency bandwidth. The pixels size of the monitor does not constitute a relevant bandwidth limiting factor effect.

III. RESULTS AND DISCUSSIONS

A. Experimental results

The average CD curves corresponding to the three standard doses of 1, 2.5, and 10 μGy are reported in Figs. 9–11. In these figures, the error bars correspond to ±1 standard error from the mean. The lines through the points are obtained by fitting the experimental data with a parabolic function (in log-log coordinates). For system C, the three smaller targets were never seen (two at low dose and one at middle dose). In those cases, fitted curves were used to extrapolate the absent data.

To test the statistical significance of the differences between the contrast detail curves of the three systems, a two factor ANOVA was performed. The main effects considered were the target size and the detector type. The results, shown in Table II, indicated that the first factor was always statistically significant while the interaction of disk size by detector type was not. At the lowest and intermediate exposure, sys-

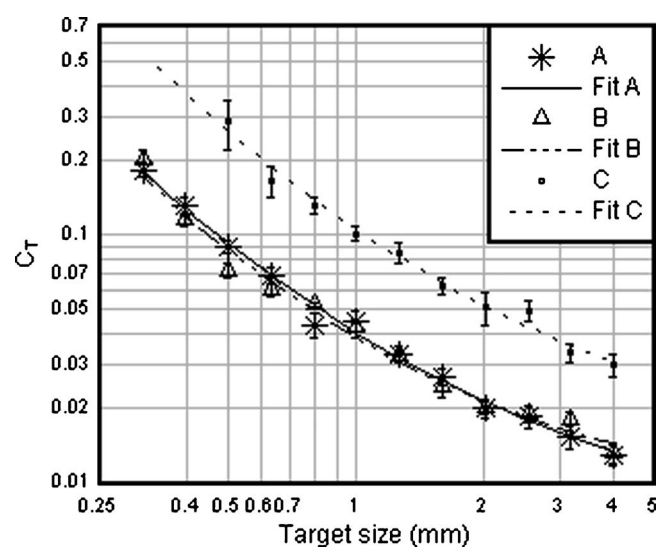

FIG. 10. Contrast detail curves for the three systems at 1 μGy. The error bars correspond to ±1 standard error from the mean. Lines through the points are obtained by fitting data with a parabolic function (in log-log coordinates). A (GE), B (Philips), and C (Hologic).

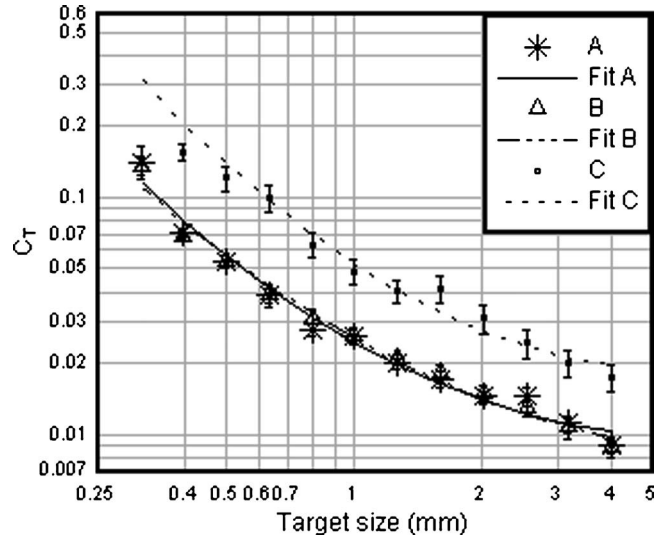

FIG. 11. Contrast detail curves for the three systems at 2.5 μGy. The error bars correspond to ±1 standard error from the mean. Lines through the points are obtained by fitting data with a parabolic function (in log-log coordinates). A (GE), B (Philips), and C (Hologic).

tems A and B were equivalent. At the highest dose, system A performed somewhat better than system B. This trend could have been expected, at least qualitatively, considering the relative DQE of the two systems. Similar results were obtained considering the two smallest targets (size 0.32 and 0.40 mm) only. For these two low contrast targets, any advantage in using a smaller pixel size was evident.

As shown by the ANOVA test reported in Table III, for each exposure level, system C exhibited a significantly lower performance in comparison to those of systems A and B. More specifically, its performance at 2.5 μGy was significantly lower than that of the indirect systems obtained at 1 μGy. At 10 μGy, the system C performance was equivalent to that obtained with the other two systems at 2.5 μGy. In this latter case, for about the same perceptibility, the direct system would require a factor four of dose increase. Referring to the 10 μGy performance of the two indirect systems, the dose level at which system B would give the same performance as system A was calculated by using the general model outlined in the Appendix. The fitting of system A experimental data by using system B specific parameters (MTF, DQE, pixel size) was obtained at dose level of 13.8 μGy ($P<0.001$).

In order to appreciate the significance of the differences observe, we further computed the minimum contrast difference that can be reliably appreciated by our CD methodology. To do so, the results from individual observers (at 2.5 μGy) were multiplied by a fixed factor and the two dataset compared using the ANOVA statistics. The two datasets could be considered statistically different ($P<0.05$) when the contrast amount difference was approximately 6%. This contrast difference would correspond to a dose variation of about 12% ($P<0.001$).

We also checked our results by changing the chosen contrast threshold (75%). Both 62.5% and the subjective minimum perceivable contrast thresholds were tried. No significant differences in the main conclusions were found.

B. Comparison with theory

The comparison between experimental and theoretical CD for the three systems is reported in Figs. 11 and 12. In all cases, the value of the (Wi/s^2) parameter (the internal eye noise divided by the squared perceived background image intensity) was found negligible ($<10^{-6}$) so that the second term in the denominator of Eq. (A8) could be dropped by the fitting procedure. This is a consequence of the visualization conditions adopted (high monitor luminance and high target contrast). As is evident looking at these figures, the model curves fit reasonably well the experimental data of the systems at different dose levels. The fitted values of the threshold signal to noise ratio (SNR_T) were 5.85±0.16 for system A, 5.65±0.14 for system B, and 7.65±0.31 for system C. Comparing systems A and B, the fitted SNR_T values were not statistically different ($P>0.1$) while C values were (P

TABLE II. (a) Two factor ANOVA test with repetitions. The response variable was the logarithm of the 75% threshold contrast. The main effects considered were the targets size and the detector type. The reported data (detector type effect) refer to six operators. (b) Two factor ANOVA test with repetitions coupling the three systems in all possible ways. The observed powers were calculated using alpha=0.05.

	Two factor ANOVA test on contrast-detail data All systems and all phantom details: main effect detector type		
	1 μGy	2.5 μGy	10 μGy
	$F(2,180)=23.81$, $p<0.001$ Observed power=0.9999	$F(2,180)=291.08$, $p<0.001$ Observed power=0.9999	$F(2,180)=169.78$, $p<0.001$ Observed power=0.9999
	Paired systems: main effect detector type		
	1 μGy	2.5 μGy	10 μGy
System A vs B	$F(1,120)=0.935$ n.s.	$F(1,120)=2.76$ n.s.	$F(1,120)=18.865$, $p<0.001$ Observed power=0.99
System B vs C	$F(1,120)=17.082$, $p<0.001$ Observed power=0.9999	$F(1,120)=350.24$, $p<0.001$ Observed power=0.9999	$F(1,120)=177.80$, $p<0.001$ Observed power=0.9999
System C vs A	$F(1,120)=18.603$, $p<0.001$ Observed power=0.9999	$F(1,120)=471.31$, $p<0.001$ Observed power=0.9999	$F(1,120)=272.82$, $p<0.001$ Observed power=0.9999

TABLE III. (a) Two factor ANOVA test with repetitions; the variable was the logarithm of the 75% threshold contrast at 10 μGy for system C compared with those at 2.5 μGy for systems A and B. (b) Two factor ANOVA test with repetitions; the variable was the logarithm of the 75% threshold contrast at 2.5 μGy for detector C in comparison with those at 1 μGy for detectors A and B. The main effects considered were the targets size and the detector type. The observed power was calculated using alpha=0.05.

Two factor ANOVA test on contrast-detail data All systems at different exposures: main effect detector type	
System A and B at 1 μGy system C at 2.5 μGy	$F(2,180)=51.44$, $p<0.001$ Observed power=0.9999
System A and B at 2.5 μGy system C at 10 μGy	$F(2,180)=1.163$ n.s.

<0.001). Related to the above-mentioned values for SNR_T, the observer efficiencies in Eq. (A8) for the three systems were $\eta_A=0.082$, $\eta_B=0.088$, and $\eta_C=0.048$.

For system A, Aufrichtig and Xue,[20] report a SNR_T value of 2.51, an internal observer's noise Wi of 1.6×10^{-5} OD mm^2, and an observer efficiency of 0.45. Apart from differences in the radiation quality (120 kVp with 12.7 cm added Plexiglas used in the prior study), the main difference in the studies is the use of soft-copy (as opposed to hard-copy) display in the present study.

IV. CONCLUSIONS

In general, indirect FPDs provided detectability and SNR_T values higher than those from the direct FPD. The differences were more that what can be expected from differences in the DQE. Following the suggestion of Moy,[44] our results suggest that aliasing is a likely cause, originated by the exceptionally high MTF of the direct systems at the Nyquist frequency.

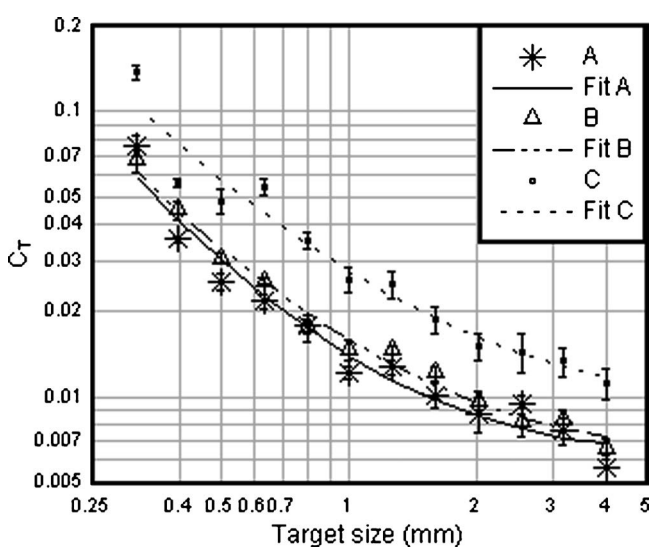

FIG. 12. Contrast detail curves for the three systems at 10 μGy. The error bars correspond to ±1 standard error from the mean. Lines through the points are obtained by fitting data with a parabolic function (in log-log coordinates). A (GE), B (Philips), and C (Hologic).

ACKNOWLEDGMENTS

The authors are deeply indebted to Ulrich Neitzel (Philips) for helpful contributions and for providing a software tool allowing the exclusion of the dose dependent "destriping" filter and the logarithmic transformation of pixel data on system B. Special thanks are due to Dr. Stefania Maggi and Dr. Edoardo Buono from Ancona Hospital and Massimo Pieroni from GE Medical for their cooperation in the evaluation of system A. The authors are also indebted to Dr. Mario Vescovi and Dr. Stefano Gagliano from RSI, Italy, for providing the GUI used to evaluate CDRAD images.

APPENDIX: THEORY OF CONTRAST DETAIL DETECTABILITY

1. Mathematical definition of the contrast detail curves

In the statistical perception (or signal detection and recognition) theory, the probability of a correct detection of signal produced by a detail (disk) in a noisy background is related to the corresponding signal-to-noise ratio (SNR). The theory links the mathematical expression of the SNR in terms of basic parameters (resolution and noise characterizing both the image and the human visual system) to the results of various detection experiments.[24,45,46] The two most important models are the ideal and the quasi-ideal observer. The ideal observer is able to use all the information in the noisy image sample, including the correlation in the noise. The quasi-ideal observer is a suboptimal observer who assumes that the noise is white, i.e., uncorrelated.

In multiple alternative forced choice (MAFC) experiments, the observer has to locate the signal in one of the M possible locations where it is randomly assigned. It is possible to demonstrate[47,48] that the probability (p) of the correct response in a M-alternative forced choice experiment for an ideal observer is related to the detectability index (d') by

$$p(d') = \int_{-\infty}^{\infty} \Phi(t)^M \cdot G(d'-t)dt, \tag{A1}$$

where $G(t)$ and $\Phi(t)$ are the Gaussian and the cumulative Gaussian functions, respectively. The "detectability index" (d') is equivalent to the image signal-to-noise ratio (SNR)

and these quantities are proportional to the image contrast C as

$$\mathrm{SNR} \equiv d' = u \cdot C, \tag{A2}$$

where

$$C = \frac{\Delta I}{I}. \tag{A3}$$

The (large area) image contrast C is defined as the relative variation of the image signal $I=I(x,y)$ produced by the target (here, and throughout the paper, a small contrast approximation is assumed). The quantity u in Eq. (A2) can be considered the SNR per unit contrast. From Eqs. (A1) and (A2), it is possible to show that the threshold contrast (at p_0 level) for a disk of diameter d, $C_T^{p_0}(d)$, is given by

$$C_T^{p_0}(d) = \frac{d'^{p_0}_{4\text{-AFC}}}{u(d)}, \tag{A4}$$

where $d'^{p_0}_{4\text{-AFC}}$ is the theoretical value for the SNR for a 4-AFC experiment. If $p_0=0.75$, $d'^{p_0}_{4\text{-AFC}}$ value is 1.68.

The real observers generally perform suboptimally corresponding to a higher threshold signal-to-noise ratio ($\mathrm{SNR_T}$) in the range of 3–7.[49] Referring to the Eq. (A4), if the quantity $u(d)$ is known from the theoretical expression of signal to noise ratio [$\mathrm{SNR}(d)$], the threshold $\mathrm{SNR_T}$ can be obtained by fitting the experimental CD curve $C_T^{p_0}(d)$ versus $\mathrm{SNR_T}/u(d)$ according to.

$$C_T^{p_0}(d) = \frac{\mathrm{SNR_T}}{u(d)}. \tag{A5}$$

A useful parameter characterizing how much the real observer approaches the ideal one in a detection task is the observer efficiency (η), defined as the squared ratio of the theoretical and the experimental signal to noise[48] is

$$\eta = \left(\frac{d'^{p_0}_M}{\mathrm{SNR_T}}\right)^2. \tag{A6}$$

2. The SNR model

As in the Aufrichtig and Xue paper,[20] it is possible to adopt a widely used model called "perceived statistical model" based on the statistical decision theory.[24,28] In our case, the task presented to the observer is to detect the presence of a disk shaped object of known size and location (signal known exactly—SKE) in a noisy background, also perfectly known (BKE). For a quasi-ideal observer, the probability of correctly detecting the object is related to the SNR expressed as

$$\mathrm{SNR} = \frac{S_p}{\sqrt{N_p^2 + N_i^2}}. \tag{A7}$$

The numerator represents the perceived power from the mean signal differential. With reference to the matched filter theory, S_p is the square root of the peak power resulting from a perfect match of the signal with the optimum filter. The denominator represents the total perceived noise and contains two terms: the first one is the image noise transferred to the observer while the second one is the internal observer noise. The latter term was introduced by Ishida *et al.* in 1984.[50] Following the derivation of Aufrichtig,[20] the SNR can be expressed as

$$\mathrm{SNR} = \frac{C \cdot F_1}{\sqrt{(F_2/\Phi) + [W_i/(s \cdot \gamma)^2]F_1}}, \tag{A8}$$

where

$$F_1 = \int_0^{fc}\int_0^{fc} |F(u,v)\mathrm{MTF}(u,v)V_s(u,v)|^2 du dv, \tag{A9}$$

$$F_2 = \int_0^{fc}\int_0^{fc} |F(u,v)\mathrm{MTF}(u,v)^2 V_s(u,v)^2|^2 \mathrm{DQE}^{-1} \cdot du dv, \tag{A10}$$

and $F(u,v)$ represents the Fourier transform of the image signal (for a disk detail, a uniform circular object of unity amplitude and diameter d). $F(u,v)$ is expressed as

$$F(u,v) = \frac{d}{2}\frac{J_1(\pi \cdot d \cdot \sqrt{u^2+v^2})}{\sqrt{u^2+v^2}}, \tag{A11}$$

where J_1 is the first order Bessel function. In Eq. (A11) the display system contrast enhancement factor γ is defined as

$$\gamma = \frac{(\Delta s/s)}{(\Delta I/I)}, \tag{A12}$$

where $\Delta s/s$ represents the (large area) contrast of the detail as reproduced by the display device, $s=s(I)$ is the large scale (average) perceived background intensity level corresponding to the image signal I, and $\Delta I/I$ is the (large area) contrast of the detail in the original image. Referring to Eq. (A8), C is the target's contrast, W_i the eye's observer's internal noise, and Φ the photon fluence.

In Eqs. (A9) and (A10), V_s is the human visual system (HVS) response function, MTF is the overall modulation transfer function of the system, and f_c, the Nyquist cut-off frequency ($f_c=1/2a$) of the system with sampling aperture and sampling distance equal to the pixel size a. If the image is displayed on a monitor with zooming, all quantities (targets' size, HVS, MTF, and f_c) are adjusted to account for the magnification at the monitor surface (see Fig. 13).

For digital detectors, otherwise to the analog ones, MTF is not "shift invariant" and depends on the position of the input modulation with respect to the pixels' position. An "expected MTF"[51] can therefore be defined as the average MTF of the imager over all possible positions of the input modulation in relation to the pixels. However, up to the proximities of the Nyquist frequency, the effective MTF is substantially the same as the presampled MTF. In this paper, we adopted as overall modulation transfer function of the system the product of the detector and display presampled MTFs. (See Figs. 14 and 15.)

Looking at Eq. (A8), it is worth noting the importance of s and γ in reducing the influence of the observer's eye's

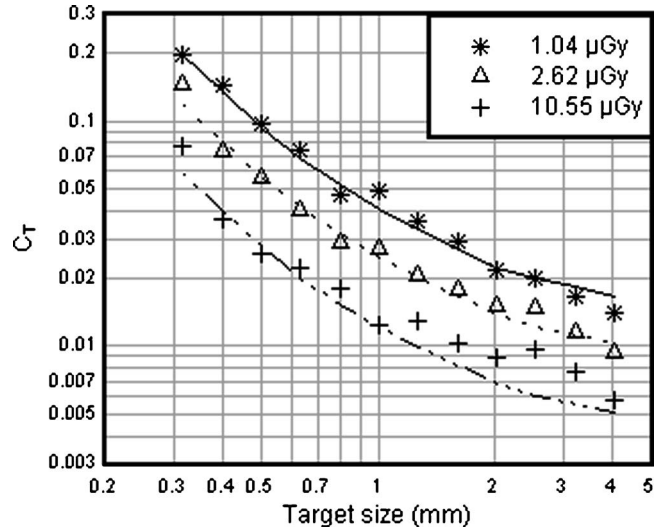

FIG. 13. System A (GE): comparison between theoretical (continuous lines) and experimental data (symbols) at three different dose levels. The fitted value for the signal to noise ratio was $SNR_T=5.85$, S.E. =0.16.

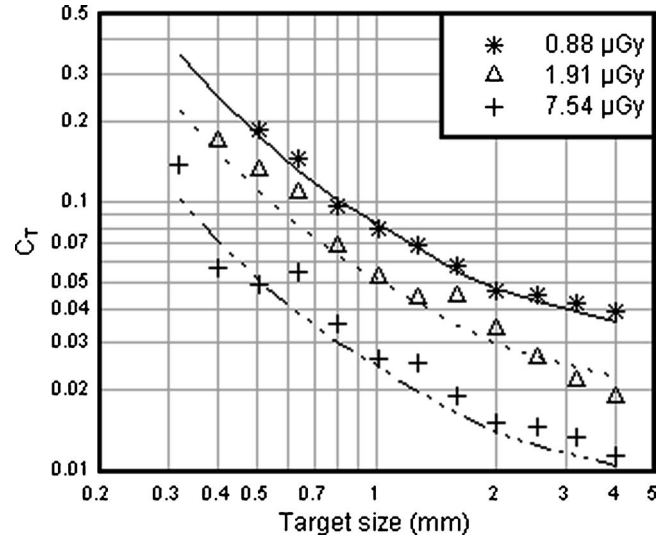

FIG. 15. System C (Hologic): comparison between theoretical (continuous lines) and experimental data (symbols) at the three different doses. The fitted value for the signal to noise ratio was $SNR_T=7.61$, S.E. =0.31.

internal noise. In a similar way, an increase of the photon fluence (Φ) or of the detector efficiency (DQE) would reduce the intrinsic image noise.

3. The psychometric function

According to the theory outlined in section A of this Appendix, the observer's response curve [i.e., the frequency of the correct response (f_k) versus the disk contrast (C_k)] should follow the Eq. (A1), which is graphically represented in Fig. 4. This function is also called psychometric (or detection) function. In our case, the experimental data exhibit significant departure from the linear trend expected by theory at the lowest contrast levels, as shown in Fig. 4 where the solid curve represents the theoretical curve fitted to the $D=0.32$ mm data. Actually only if the observer acts in an ideal way (as suggested by de Vries[52] and Rose[53]), the detectability d' would be proportional to signal contrast.[54] However, d' increases with the contrast with a power greater than unity.[55–59] The temporal and spatial uncertainty of the signal may explain this effect.[31,55,60] For this reason, the psychometric functions for the visual contrast detection have been described by sigmoid curves.[31,34] In this paper, the psychometric functions is described by the best fitting (of parameters u and β) of a Weibull function[31] as

$$p(c) = 1 - (1 - \gamma) \cdot e^{[-(u \cdot c)^{\beta}]}, \tag{A13}$$

with $\gamma=0.25$ for a 4-AFC experiment.

The dotted and dashed curves in Fig. 4 are obtained by fitting this function to experimental data, using the maximum likelihood method based on binomial statistics, as described by Ohara *et al.*[47] It was observed that, in general, the threshold contrast $C_T^{p_0}(d)$ corresponding to $p_0=0.75$ is not too critically dependent on the shape of the fitting function; as shown in Fig. 4, even the linear model would give an estimate of $C_T^{p_0}(d)$ not too far from that obtained using the Weibull function.

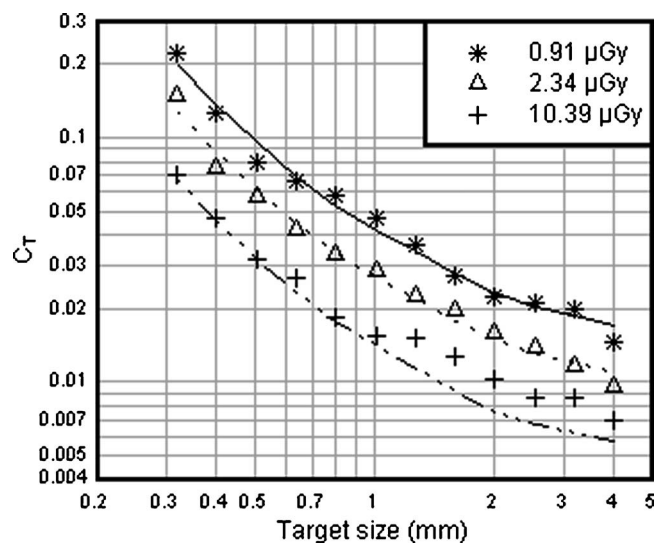

FIG. 14. System B (Philips): comparison between theoretical (continuous lines) and experimental data (symbols) at the three different doses. The fitted value for the signal to noise ratio was $SNR_T=5.65$, S.E. =0.14.

[a]Electronic mail: gianni.borasi@asmn.re.it

[1]M. Sonoda, M. Takano, J. Miyahara, and H. Kato, "Computed radiography utilizing scanning laser stimulated luminescence," Radiology **148**, 833–838 (1983).
[2]E. Samei and M. J. Flynn, "An experimental comparison of detector performance for computed radiography systems," Med. Phys. **29**, 447–459 (2002).
[3]A. Karellas, L. J. Harris, H. Liu, M. A. Davis, and C. J. D'Orsi, "Charge-coupled device detector: performance considerations and potential for small-field mammographic imaging applications," Med. Phys. **19**, 1015–1023 (1992).
[4]S. Hejazi and D. P. Trauernicht, "System considerations in CCD-based x-ray imaging for digital chest radiography and digital mammography," Med. Phys. **24**, 287–297 (1997).
[5]U. Neitzel, I. Maack, and S. Gunther-Kohfahl, "Image quality of a digital chest radiography system based on a selenium detector," Med. Phys. **21**,

509–516 (1994).
[6]J. H. Launders, S. M. Kengyelics, and A. R. Cowen, "A comprehensive physical image quality evaluation of a selenium based digital x-ray imaging system for thorax radiography," Med. Phys. **25**, 986–997 (1998).
[7]M. J. Yaffe and J. A. Rowlands, "X-ray detectors for digital radiography," Phys. Med. Biol. **42**, 1–39 (1997).
[8]D. L. Lee, L. K. Cheung, B. G. Rodricks, and G. F. Powell, "Improved imaging performance of a 14×17-inch digital radiography system using Se/TFT detector," Proc. SPIE **3336**, 14–23 (1998).
[9]W. Zhao, I. Blevis, S. Germann, J. A. Rowlands, D. Waechter, and Z. Huang, "Digital radiology using active matrix readout of amorphous selenium: construction and evaluation of a prototype real-time detector," Med. Phys. **24**, 1834–1843 (1997).
[10]J. H. Siewerdsen, L. E. Antonuk, Y. el-Mohri, J. Yorkston, W. Huang, J. M. Boudry, and I. A. Cunningham, "Empirical and theoretical investigation of the noise performance of indirect detection, active matrix flat-panel imagers (AMFPIs) for diagnostic radiology," Med. Phys. **24**, 71–89 (1997).
[11]C. Chaussat, J. Chabbal, T. Ducurant, V. Spinnler, G. Vieux, and R. Neyret, "New CsI/a-Si 17"x17" x-ray flat-panel detector provides superior detectivity and immediate direct digital output for general radiography systems," Proc. SPIE **3336**, 45–56 (1998).
[12]F. Fischbach, T. Freund, R. Rottgen, U. Engert, R. Felix, and J. Ricke, "Dual-energy chest radiography with a flat-panel digital detector: revealing calcified chest abnormalities," AJR, Am. J. Roentgenol. **181**, 1519–1524 (2003).
[13]J. Dobbins III and D. J. Godfrey, "Digital x-ray tomosynthesis: current state of the art and clinical potential," Phys. Med. Biol. **48**, R65–106 (2003).
[14]P. R. Granfors and R. Aufrichtig, "Performance of a 41X41-cm2 amorphous silicon flat panel x-ray detector for radiographic imaging applications," Med. Phys. **27**, 1324–1331 (2000).
[15]J. R. Floyd CE, R. J. Warp, J. Dobbins III, H. G. Chotas, A. H. Baydush, R. Vargas-Voracek, and C. E. Ravin, "Imaging characteristics of an amorphous silicon flat-panel detector for digital chest radiography," Radiology **218**, 683–688 (2001).
[16]H. G. Chotas and C. E. Ravin, "Digital chest radiography with a solid-state flat-panel x-ray detector: contrast-detail evaluation with processed images printed on film hard copy," Radiology **218**, 679–682 (2001).
[17]X. J. Rong, C. C. Shaw, X. Liu, M. R. Lemacks, and S. K. Thompson, "Comparison of an amorphous silicon/cesium iodide flat-panel digital chest radiography system with screen/film and computed radiography systems–a contrast-detail phantom study," Med. Phys. **28**, 2328–2335 (2001).
[18]M. Uffmann, C. Schaefer-Prokop, U. Neitzel, M. Weber, C. J. Herold, and M. Prokop, "Skeletal applications for flat-panel versus storage-phosphor radiography: Effect of exposure on detection of low-contrast details," Radiology **231**, 506–514 (2004).
[19]R. Aufrichtig, "Comparison of low contrast detectability between a digital amorphous silicon and a screen-film based imaging system for thoracic radiography," Med. Phys. **26**, 1349–1358 (1999).
[20]R. Aufrichtig and P. Xue, "Dose efficiency and low-contrast detectability of an amorphous silicon x-ray detector for digital radiography," Phys. Med. Biol. **45**, 2653–2669 (2000).
[21]E. Samei, M. J. Flynn, H. G. Chotas, and J. T. Dobbins III, "DQE of direct and indirect digital radiographic systems," Proc. SPIE **4320**, 189–197 (2001).
[22]E. Samei and M. J. Flynn, "An experimental comparison of detector performance for direct and indirect digital radiography systems," Med. Phys. **30**, 608–622 (2003).
[23]G. Borasi, A. Nitrosi, P. Ferrari, and D. Tassoni, "On site evaluation of three flat panel detectors for digital radiography," Med. Phys. **30**, 1719–1731 (2003).
[24]R. F. Wagner and D. G. Brown, "Unified SNR analysis of medical imaging systems," Phys. Med. Biol. **30**, 489–518 (1985).
[25]G. Pedroli, A. Crespi, C. Ghezzi, G. Montanari, N. Paruccini, E. Salvini, and M. Tagliabue, "Evaluation of a psychophysical model of observer performance in the detection of low contrast radiographic patterns," Physica Medica **XIII**, 339–343 (1997).
[26]H. Chan, C. Metz, and K. Doi, "Digital image processing: optimal spatial filter for maximization of the perceived SNR based on a statistical decision theory model for the human observer.," Proc. SPIE **535**, 2–11 (1985).
[27]M. A. O. Thijssen, K. R. Bijkerk, and R. J. M. van der Burght, *Manual Contrast-Detail Phantom CDRAD Type 2.0: Project Quality Assurance in Radiology* (Department of Radiology, University Hospital Nijmegen, St. Radboud, The Netherlands, 1998).
[28]IEC 61267, *Medical Diagnostic X-ray Equipment - Radiation Conditions for Use in the Determination of Characteristics*, 1st ed. (IEC Publication, Geneva, Switzerland, 1994).
[29]IEC 61223-2-5, *Evaluation and Routine Testing in Medical Imaging Departments. Part 2-5: Constancy Tests—Image Display Devices* (*Commission Internationale de l'Eclairage* (*CIE*), Wien, Austria, 1994).
[30]S. Suryanarayanan, A. Karellas, S. Vedantham, S. M. Waldrop, C. J. D'Orsi, S. Suryanarayanan, A. Karellas, S. Vedantham, H. Ved, S. P. Baker, and C. J. D'Orsi, "A perceptual evaluation of JPEG 2000 image compression for digital mammography: contrast-detail characteristics.; Flat-panel digital mammography system: contrast-detail comparison between," J. Digit Imaging **17; 225**, 801–807 (2004).
[31]D. G. Pelli, "Uncertainty explains many aspects of visual contrast detection and discrimination," J. Opt. Soc. Am. A **2**, 2–26 (1985).
[32]A. Rose, "A unified approach to the performance of photographic film, television pick up tubes and human eye," J. Soc. Motion Pict. Eng. **47**, 196–208 (1946).
[33]S. Siegel, *Nonparametric Statistics for the Behavioral Sciences* (McGraw-Hill, New York, 1956).
[34]S. Suryanarayanan, A. Karellas, S. Vedantham, H. Ved, S. P. Baker, and C. J. D'Orsi, "Flat-panel digital mammography system: contrast-detail comparison between screen-film radiographs and hard-copy images," Radiology **225**, 801–807 (2002).
[35]G. W. Snedecor and W. G. Cochran, *Statistical Methods*, 6th ed. (Iowa State University Press, Ames, Iowa, 1967).
[36]P. R. Bevington, *Data Reduction and Error Analysis for the Physical Sciences* (McGraw-Hill, New York, 1969).
[37]U. Neitzel, S. Gunther-Kohfahl, G. Borasi, and E. Samei, "Determination of the detective quantum efficiency of a digital x-ray detector: Comparison of three evaluations using a common image data set," Med. Phys. **31**, 2205–2211 (2004).
[38]P. Monnin, D. Gutierrez, S. Bulling, D. Lepori, J. F. Valley, and F. R. Verdun, "Performance comparison of an active matrix flat panel imager, computed radiography system, and a screen-film system at four standard radiation qualities," Med. Phys. **32**, 343–350 (2005).
[39]H. Illers, E. Buhr, D. Bergmann, and C. Hoeschen, "Measurement of the detective quantum efficiency (DQE) of digital x-ray imaging devices according to the standard IEC 62220-1," Proc. SPIE **5368**, 177–187 (2004).
[40]H. Blume, P. Steven, M. Cobb, A. M. Ho, F. Stevens, M. S. H. Roherig, and J. Fan, "Characterization of high-resolution liquid-crystal displays for medical images," Proc. SPIE **4681**, 23–28 (2002).
[41]F. L. Van Nes and M. A. Bouman, "Spatial Modulation Transfer in the Human Eye," J. Opt. Soc. Am. **57**, 401–406 (1967).
[42]K. D. H. Kelly, "Visual contrast sensitivity," Opt. Acta **24**, 107–129 (1977).
[43]G. J. Barten, "Physical model for the contrast sensitivity of the human eye," Proc. SPIE **1666**, 57–72 (1992).
[44]J. P. Moy, "Signal-to-noise ratio and spatial resolution in x-ray electronic imagers: Is the MTF a relevant parameter?," Med. Phys. **27**, 86–93 (2000).
[45]J. A. Sweets and R. Pickett, *Evaluation of Diagnostic Systems* (Academic, New York, 1982).
[46]N. A. Macmillan and C. D. Creelman, *Detection Theory: A User's Guide*, (Cambridge University, New York, 1991).
[47]K. Ohara, K. Doi, C. E. Metz, and M. L. Giger, "Investigation of basic imaging properties in digital radiography. 13. Effect of simple structured noise on the detectability of simulated stenotic lesions," Med. Phys. **16**, 14–21 (1989).
[48]A. E. Burgess, "Comparison of receiver operating characteristic and forced choice observer performance measurement methods," Med. Phys. **22**, 643–655 (1995).
[49]A. E. Burgess, "The Rose model, revisited," J. Opt. Soc. Am. A **16**, 633–645 (1999).
[50]M. Ishida, K. Doi, L. N. Loo, C. E. Metz, and J. L. Lehr, "Digital image processing: Effect on detectability of simulated low-contrast radiographic patterns," Radiology **150**, 569–575 (1984).
[51]J. Dobbins III, "Effects of undersampling on the proper interpretation of modulation transfer function, noise power spectra, and noise equivalent quanta of digital imaging systems," Med. Phys. **22**, 171–181 (1995).

[52]H. de Vries, "The quantum character of light and its bearing upon threshold of vision, the differential sensitivity and visual acuity of the eye.," Physica (Amsterdam) **10**, 553–564 (1943).
[53]A. Rose, "The sensitivity performance of the human eye on an absolute scale," J. Opt. Soc. Am. **38**, 196–208 (1948).
[54]D. Green and J. A. Swets, *Signal Detection Theory and Psychophysics* (Wiley, New York, 1966).
[55]W. P. Tanner, "Physiological implication of psycophysical data," Ann. N.Y. Acad. Sci. **89**, 752–765 (1961).
[56]J. Nachmias and E. C. Kocher, "Visual detection and discrimination of luminous increments," J. Opt. Soc. Am. **60**, 382–389 (1970).
[57]J. Nachmias and R. Sansbury, "Grating contrast: discrimination may be better than detection," Vision Res. **14**, 1039–1042 (1971).
[58]T. Cohn, L. Thibos, and R. N. Kleinstein, "Detectability of a luminance increment," J. Opt. Soc. Am. **64**, 1321–1327 (1974).
[59]J. Nachmias, "On the psychometric function for contrast detection," Vision Res. **21**, 215–223 (1981).
[60]M. Eckstein, A. J. Ahumada Jr, and A. B. Watson, "Visual signal detection in structured backgrounds. II. Effects of contrast gain control, background variation, and white noise.," J. Opt. Soc. Am. A **14**, 2406–2419 (1997).